Research article

Cheng Zong and Ji-Xin Cheng*

Origin of dispersive line shapes in plasmon-enhanced stimulated Raman scattering microscopy

https://doi.org/10.1515/nanoph-2020-0313
Received June 3, 2020; accepted June 29, 2020; published online July 27, 2020

Abstract: Plasmon-enhanced stimulated Raman scattering (PESRS) microscopy has been recently developed to reach single-molecule detection limit. Unlike conventional stimulated Raman spectra, dispersive-like vibrational line shapes were observed in PESRS. Here, we propose a theoretical model together with a phasor diagram to explain the observed dispersive-like line shapes reported in our previous study. We show that the local enhanced electromagnetic field induced by the plasmonic nanostructure interferes with the molecular dipole-induced field, resulting in the dispersive profiles of PESRS. The exact shape of the profile depends on the phase difference between the plasmonic field and the molecular dipole field. We compared plasmon-enhanced stimulated Raman loss (PESRL) and plasmon-enhanced stimulated Raman gain (PESRG) signals under the same pump and Stokes laser wavelength. The PESRL and PESRG signals exhibit similar signal magnitudes, whereas their spectral line shapes show reversed dispersive profiles, which is in an excellent agreement with our theoretical prediction. Meanwhile, we verify that the nonresonant background in PESRS mainly originates from the photothermal effect. These new insights help the proper use of PESRS for nanoscale bioimaging and ultrasensitive detection.

Keywords: plasmon; plasmon-enhanced spectroscopy; stimulated Raman scattering.

***Corresponding author: Ji-Xin Cheng**, Department of Electrical and Computer Engineering, Boston University, Boston, MA 02215, USA; Department of Biomedical Engineering, Boston University, Boston, MA 02215, USA; Photonics Center, Boston University, Boston, MA 02215, USA; and Department of Chemistry, Boston University, Boston, MA 02215, USA, E-mail: jxcheng@bu.edu. https://orcid.org/0000-0003-2048-6207
Cheng Zong: Department of Electrical and Computer Engineering, Boston University, Boston, MA 02215, USA, E-mail: czongcz@bu.edu

1 Introduction

Raman spectroscopy offers label-free contrasts for bioimaging based on the vibrational information of biomolecules such as lipids, protein, DNA, and small metabolites [1]. However, spontaneous Raman spectroscopy suffers from its poor sensitivity due to inherent small cross-sections for most endogenous biomolecules. It needs a long exposure time to obtain a high-quality Raman spectrum. Owing to the generation of a coherent light field, stimulated Raman scattering (SRS) produces a signal that is many orders of magnitude larger than that of spontaneous Raman spectroscopy [2]. Because of its fast imaging speed comparable with fluorescence microscopy, SRS microscopy has been extensively utilized to capture chemical images of live cells, large-area tissues, living animals, and even human subjects [3].

Despite these attractive attributions, the imaging sensitivity of SRS is not sufficient for performing measurements on the single-molecule level without other enhancement processes [2]. To detect SRS signals from a single molecule, one approach is the involvement of electronic resonance which increases the nonlinear susceptibility of a molecule. Min and coworkers reported electronic pre-resonance SRS to achieve sub-micromolar-sensitivity detection for chromophores [4, 5]. Later, Min et al. reported a stimulated Raman excited fluorescence method that encoded the vibrational resonance into the fluorescence emission. This approach can obtain the Raman signal of the single chromophore by detecting its fluorescence signal [6]. Another route to achieving single-molecule detection is to enlarge the driving light field. Due to the localized surface plasmon resonance (LSPR) effect, the plasmonic nanostructure dramatically increases the intensity of the local electromagnetic field on and near the metal surface [7, 8]. The local enhanced electromagnetic field interacts with molecules close to the nanostructure surface to amplify the SRS signals. The Van Duyne's group reported surface-enhanced femtosecond SRS (SE-FSRS) spectra, including stimulated Raman loss (SRL) and stimulated Raman gain (SRG) from molecules embedded in a SiO_2-coated gold

nanodumbbell colloid [9–12]. Very recently, Cheng and coworkers demonstrated a label-free plasmon-enhanced SRS (PESRS) microscopy which is able to detect single molecules having extremely small Raman cross-sections (~10^{-30} cm^2 sr^{-1}) with the aid of gold nanoparticles (Au NPs) and the pico-Joule high-repetition-rate laser pulses [13]. The reported PESRS microscopy opened a new window for ultrasensitive and ultrafast bio-imaging.

Unlike the Lorentzian-line shape in traditional SRS spectroscopy, SE-FSRS spectroscopy and PESRS hyperspectral imaging both produced dispersive line shape spectra [9–15]. The dispersive line shape was attributed to Fano interference of the discrete molecular vibrational states on the continuum-like plasmon resonance [9, 11]. Ziegler et al. indicated that the cross term between the heterodyned SE-FSRS signal and the plasmon light emission resulted in the dispersive-like line shape [16]. Schatz et al. proposed that the asymmetric line shape resulted from the combination of two Fano contributions arising from the interference between both the real and imaginary components of the Raman local electromagnetic field and the plasmon field [17]. Both theoretical descriptions were based on reported SE-FSRS results and only discussed the SRG process. Yet, there are significant differences between the SE-FSRS measurement and PESRS imaging in experiment conditions, including the laser pulse duration, the modulation frequency, the laser excitation, collection approach, and the data processing. Besides, the recent wavelength-dependent SE-FSRS result did not match predictions of any proposed SE-FSRS theory, indicating an incomplete understanding of the plasmon-enhanced SRS process [12, 18].

In this article, we employ the classic light-matter interaction theory and the phasor diagram to elucidate the origin of dispersive shapes in plasmon-enhanced stimulated Raman loss (PESRL) and plasmon-enhanced stimulated Raman gain (PESRG) measurements. The phasor graphs provide an intuitive view of the origin of dispersion, which derives from an interaction between the plasmon-enhanced electric field and the molecular dipole field. We also develop a theoretical model to simulate both PESRL and PESRG spectra. Furthermore, PESRL and PESRG measurements using the same pump and Stokes laser wavelength are conducted to confirm our theoretical prediction.

2 Theory

We start with basic SRS in the absence of a plasmonic field. For details on the classical model of the SRS process, readers can read references [19, 20]. Assuming a pump field (E_P) at the frequency of ω_P and a Stokes field (E_S) at the frequency of ω_S. Based on heterodyne detection, the SRL and SRG intensities can be written as

$$I_{\mathrm{SRL}} = 2\mathrm{Re}\left[E_P^* E_{\mathrm{SRL}}\right] \tag{1a}$$

$$I_{\mathrm{SRG}} = 2\mathrm{Re}\left[E_S^* E_{\mathrm{SRG}}\right] \tag{1b}$$

where

$$E_{\mathrm{SRL}} = i\chi_{\mathrm{SRL}} E_S E_P E_S^* \tag{2a}$$

$$E_{\mathrm{SRG}} = i\chi_{\mathrm{SRG}} E_P E_S E_P^* \tag{2b}$$

and

$$\chi_{\mathrm{SRL}} = \chi_{\mathrm{NR}} + \frac{\alpha}{\delta - i\Gamma} \tag{3a}$$

$$\chi_{\mathrm{SRG}} = \chi_{\mathrm{NR}} + \frac{\alpha}{\delta + i\Gamma} \tag{3b}$$

Here $\delta = \Omega_v - (\omega_P - \omega_S)$, Γ is the half width at height maximum (HWHM). α is the oscillator strength of the molecular vibration. Ω_v is the Raman vibrational frequency. As shown in Figure S1, the imaginary part of χ_R shows a Lorentzian form, whereas the real part features a Fano dispersive profile [20]. We note that χ_{NR}, a constant, is contributed by the cross-phase modulation (XPM), the photothermal effect (PT), or the transient absorption (TA), which could be minimized after optimizing the optical design [21].

For SRL, the first term and second term in χ_{SRL} produce a non-Raman resonant field ($E_{\mathrm{SRL}}^{\mathrm{NR}}$) and a Raman resonant field (E_{SRL}^{R}), respectively. In a phasor representation for SRL, we set the local oscillator E_P as a reference field with zero phases ($E_P = 1$). The SRL intensity is a projection of E_{SRL} on the x-axis. As shown in Figure 1a, $E_{\mathrm{SRL}}^{\mathrm{NR}}$ has a $\pi/2$ phase shift from E_P and therefore is decoupled from E_P. E_{SRL}^{R} has an additional phase shift θ from $E_{\mathrm{SRL}}^{\mathrm{NR}}$, with $\theta = tg^{-1}(\Gamma/\delta)$. Thus, only E_{SRL}^{R} is coupled to E_P and the x-axis projection of E_{SRL}^{R} (the imaginary part of χ_{SRL}) produces an intensity loss in the pump beam. For SRG, E_S is set as a reference field with zero phase ($E_s = 1$). $E_{\mathrm{SRG}}^{\mathrm{NR}}$ is decoupled from E_S, and E_{SRG}^{R} is coupled to E_S as shown in Figure 1b. The x-axis projection of E_{SRG}^{R} (the imaginary part of χ_{SRG}) generates an intensity gain in the Stokes beam due to a phase shift $\theta = tg^{-1}(-\Gamma/\delta)$ between E_{SRG}^{R} and $E_{\mathrm{SRG}}^{\mathrm{NR}}$. Both SRL and SRG show a Lorentzian line shape.

In the case of PESRS, the signal is from the interaction of a molecule with the local enhanced electromagnetic field. Thus, the PESRS intensity is rewritten as:

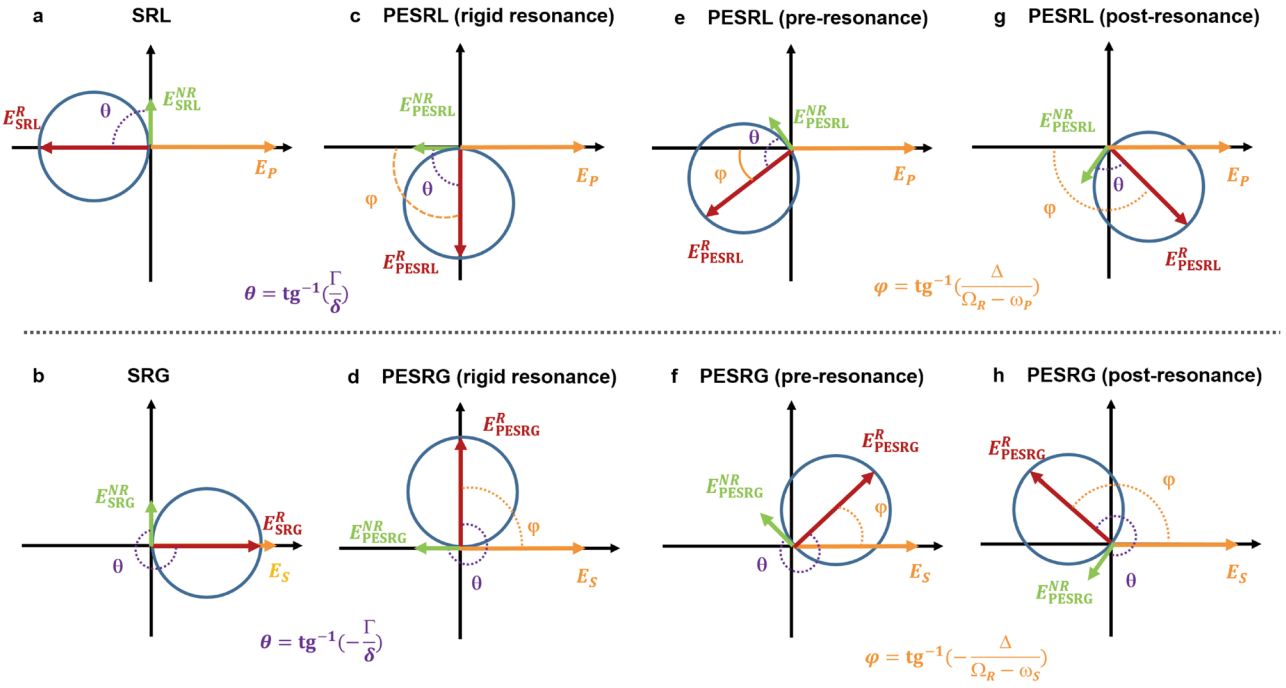

Figure 1: Phasor graphs of stimulated Raman scattering (SRS) and plasmon-enhanced stimulated Raman scattering (PESRS). Phasor representation of stimulated Raman loss (SRL) (a) and stimulated Raman gain (SRG) (b) without plasmon field, plasmon-enhanced stimulated Raman loss (PESRL) (c) and plasmon-enhanced stimulated Raman gain (PESRG) (d) at rigid plasmon resonance, PESRL (e) and PESRG (f) at plasmon pre-resonance, and PESRL (g) and PESRG (h) at plasmon post-resonance. E_P and E_S are set as a reference field with zero phase.

$$I^{\mathrm{PE}}_{\mathrm{SRL}} = 2\mathrm{Re}\left[E^*_P E_{\mathrm{PESRL}}\right] \tag{4a}$$

$$I^{\mathrm{PE}}_{\mathrm{SRG}} = 2\mathrm{Re}\left[E^*_S E_{\mathrm{PESRG}}\right] \tag{4b}$$

where

$$E_{\mathrm{PESRL}} = i\chi_{\mathrm{SRL}} E^{\mathrm{PE}}_S E^{\mathrm{PE}}_P E^{\mathrm{PE}*}_S \tag{5a}$$

$$E_{\mathrm{PESRG}} = i\chi_{\mathrm{SRG}} E^{\mathrm{PE}}_P E^{\mathrm{PE}}_S E^{\mathrm{PE}*}_P \tag{5b}$$

Here, the local enhancement fields are described as $E^{\mathrm{PE}}_P = E_P F_P$ and $E^{\mathrm{PE}}_S = E_S F_S$. The plasmon enhancement coefficient is given by [22],

$$F_P = 1 + \frac{A\Delta}{\Omega_R - \omega_P - i\Delta} \tag{6a}$$

$$F_S = 1 + \frac{A\Delta}{\Omega_R - \omega_S - i\Delta} \tag{6b}$$

where Ω_R is the LSPR frequency, Δ is the HWHM of plasmon peak with the Lorentzian shape, and A is the local field enhancement factor. When the pump and Stokes fields are tuned to near plasmon resonance and A is large enough, the first term in eq. (6) can be ignored. Thus, E^{PE}_P and E^{PE}_S express a phase shift of $\varphi_P = tg^{-1}(\Delta/\Omega_{\mathrm{R}} - \omega_P)$ and $\varphi_S = tg^{-1}(\Delta/\Omega_{\mathrm{R}} - \omega_S)$ from the E_P and the E_S field, respectively, in the phasor representation. The φ_P and the φ_S are transferred to the signal field E_{PESRL} and E_{PESRG}, respectively. The cases of plasmon rigid resonance ($\varphi_P = \varphi_S = \pi/2$) are shown in Figure 1c and d. The phasor representations of E_{PESRL} and E_{PESRG} both show a $\pi/2$ anticlockwise rotation about the origin E_{SRL} and the E_{SRG} field, respectively. For PESRL, both E^R_{PESRL} and $E^{\mathrm{NR}}_{\mathrm{PESRL}}$ are coupled to the local oscillator E_P. The $E^{\mathrm{NR}}_{\mathrm{PESRL}}$ generates an intensity loss in the pump beam. The x-axis projection of E^R_{PESRL} (the real part of χ_{SRL}) produces an intensity loss in the pump beam at the lower wavenumber region and an intensity gain in the pump beam at the higher wavenumber region. Similarly, for PESRG, E^R_{PESRG} and $E^{\mathrm{NR}}_{\mathrm{PESRG}}$ are coupled to the local oscillator E_S. The $E^{\mathrm{NR}}_{\mathrm{PESRG}}$ generates an intensity loss in the Stokes beam. The x-axis projection of E^R_{PESRG} (the real part of χ_{SRG}) generates an intensity gain in the Stokes beam at the lower wavenumber region and generates an intensity loss at the higher wavenumber region. Notably, the x-axis projections of E^R_{PESRL} and E^R_{PESRG} are zero at the Raman resonance ($\omega_P - \omega_S = \Omega_v$) condition.

Figure 1e and f presents the pre-resonance conditions ($\Omega_{\mathrm{R}} - \omega_P > 0$ or $\Omega_{\mathrm{R}} - \omega_S > 0$). For PESRL, since the nonresonant background and the SRL signal are largely on the left side of y axis, the total intensity change in the pump beam should appear as a sum of the stimulated Raman signal and the nonresonant background. For PESRG, since the nonresonant background and the SRL signal are mostly on the

opposite side of y axis, the total intensity change in the Stokes beam appears as a subtraction of the stimulated Raman signal from the nonresonant background. At the plasmonic post-resonance condition ($\Omega_R - \omega_P < 0$ or $\Omega_R - \omega_S < 0$), we predict a gain in pump beam and a loss in Stokes beam, as shown in Figure 1g and h.

Next, we discuss the origin of the nonresonant background in the PESRS microscopy. As shown in Figure S2, a strong nonresonant background, in the form of an intensity loss, is generated in the Au NPs substrates with and without adenine adsorption. The background also shows a broad and asymmetric profile in a delay time domain. Moreover, the strong backgrounds are observed in the negative delay time region. Thus, we assign the nonresonant background to the PT effect of Au NPs. The PT effect can be viewed as a scattering field ($E_{PT} \propto \Delta n V E_{pr} \propto \sigma_{abs} E_{heat}^2 E_{pr}$) induced by an equivalent dipole [23–25]. Here, E_{heat} is the heat laser (the modulated laser) field and E_{pr} is the probe laser field. σ_{abs} is the wavelength-depended absorption cross-section of Au NPs, which depends on the plasmon profiles [26]. Thus, the PT signal intensity (I_{PT}) corresponds to the interference of the scattering field with the incident probe beam (E_{pr}) as following [23]:

$$I_{PT} = 2\mathrm{Re}\left[E_{pr}^* E_{PT}\right] = C\sigma_{abs}|E_{heat}|^2|E_{pr}|^2 \tag{7a}$$

$$\sigma_{abs} = \frac{A\Delta^2}{(\Omega_R - \omega_{heat})^2 + \Delta^2} \tag{7b}$$

Here, C is a constant which reflect the magnitude of PT contribution. We note that other pump-probe processes including XPM and TA may also contribute a small part of nonresonant background. Both XPM and TA can be considered to be wavelength independent [21], which does not impact the dispersive line shapes of PESRL and PESRG.

By inserting eq. (5) into eq. (4) and adding the PT contribution (eq. (7)), a full expression of PESRS is given by

$$\begin{aligned} I_{SRL}^{PE} &= I_{PT} - 2\mathrm{Re}\left(E_P^* E_{SRL}^{PE}\right) = I_{PT} - 2\mathrm{Re}\left(E_P^* i\chi_{SRL} E_P^{PE}\right)|E_S^{PE}|^2 \\ &= I_{PT} - 2|E_S F_S|^2|E_P|^2\left[\mathrm{Im}(F_P)\mathrm{Re}(\chi_{SRL}) + \mathrm{Re}(F_P)\mathrm{Im}(\chi_{SRL})\right] \end{aligned} \tag{8a}$$

$$\begin{aligned} I_{SRG}^{PE} &= I_{PT} + 2\mathrm{Re}\left(E_S^* E_{SRG}^{PE}\right) = I_{PT} + 2\mathrm{Re}\left(E_S^* i\chi_{SRG} E_S^{PE}\right)|E_P^{PE}|^2 \\ &= I_{PT} + 2|E_P F_P|^2|E_S|^2\left[\mathrm{Im}(F_S)\mathrm{Re}(\chi_{SRG}) + \mathrm{Re}(F_S)\mathrm{Im}(\chi_{SRG})\right] \end{aligned} \tag{8b}$$

The PESRS can be viewed as a linear combination of an asymmetric line shape (the real part of molecular susceptibility) and a symmetric line shape (the imaginary part of molecular susceptibility). The dispersive line shape of PESRS depends on the relative contribution of the imaginary and real components of the plasmonic field. The PT term normally is a negative constant value in a short spectral window. As shown in eq. (8), the interference between the molecular susceptibility and the plasmon enhancement coefficient leads to the dispersive line shapes in PESRS. When $I_{PT} = 0$ and $F_P = F_S = 1$ (no plasmon resonance), eq. (8) is reduced to the normal SRG and SRL cases.

We performed simulations of PESRS based on eq. (8). The Raman peak is centered at 731 cm^{-1} with a 7 cm^{-1} HWHM. The pump and Stokes beam wavelengths are centered at 969 nm and 1040 nm, respectively. The plasmon peak is kept at 800 nm. The HWHM of the plasmonic peak is set as 5000 cm^{-1}. The PT constant C is set

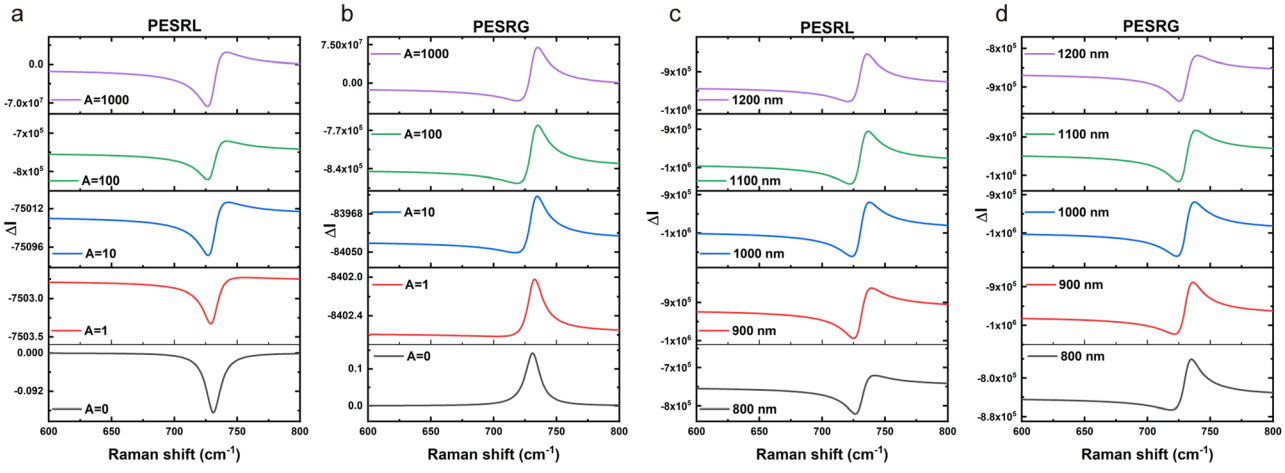

Figure 2: Simulation results. (a–b) Simulated plasmon-enhanced stimulated Raman loss (PESRL) (a) and plasmon-enhanced stimulated Raman gain (PESRG) (b) as a function of the plasmonic enhancement factor, A. The plasmon peak is kept at 800 nm. (c–d) Simulated PESRL (c) and PESRG (d) as a function of the plasmon peak Ω_R and enhancement factor is kept at 100. For all simulations, the pump and Stokes beam wavelengths are centered at 969 nm and 1040 nm, respectively. The Raman peak is centered at 731 cm^{-1} with an half width at height maximum (HWHM) of 7 cm^{-1}. The photothermal effect (PT) constant C is set as −10,000.

as –10,000, indicating an intensity loss in the probe beam. The simulated PESRL and PESRG results are shown in Figure 2. Figure 2a and b presents the PESRL and PESRG spectra as a function of the enhancement factor A. As we expected, without plasmon enhancement ($A = 0$), the SRL and SRG spectral profiles are determined by the imaginary part of χ, both showing symmetric Lorentzian-line shapes with a negative and a positive peak, respectively. With the plasmonic effect, SRL and SRG both show dispersive line shapes. All PESRL spectra show a strong negative peak at lower wavenumber and a weak positive peak at higher wavenumber. All PESRG spectra show a strong positive peak at higher wavenumber and a weak dip at lower wavenumber. As we predicted, the asymmetric profiles of PESRL and PESRG are opposite. In addition, PESRL and PESRG acquire more prominent dispersive characters as the enhancement factor increases. Similar results were reported by Ziegler [16]. While we find that the dispersive characters do not increase when the enhancement factor reaches a point that is large enough. As we discussed above, the dispersive line shape depends on the plasmon resonance frequency relative to the pump/Stokes frequency. As is evident in Figure 2c and d, the increasing dispersive line shapes and more negative PT backgrounds are shown when the plasmonic peak approaches the pump or Stokes wavelength. Intriguingly, under the plasmon post-resonance condition (e.g., first rows in the panel c and d), as predicted by our phasor diagram, PESRL appears as a gain at post-resonance condition, i.e., the positive peak becomes stronger than the negative peak. Similarly, PESRG appears as a loss, i.e., the negative peak dominates.

3 Result and discussion

We have experimentally investigated the line shapes of PESRL and PESRG predicted by our theoretical model above. The hyperspectral SRS data are collected by using a spectral-focusing SRS microscope which has been previously described [13]. Figure 3 presents the scheme of the hyperspectral SRS microscope. In brief, an 80 MHz tunable femtosecond laser (InSight DS+, Spectra-Physics) provides the pump (969 nm, ~120 fs) and Stokes (1040 nm, ~200 fs) lasers. Two acousto-optic modulators are installed in the pump and the Stokes beams for implementing SRL and SRG, respectively. The pump and the Stokes beams are collinearly overlapped and sent to an upright microscope with a 2D galvo mirror system for the laser scanning. To obtain spectral-domain information, the pump and the Stokes pulses are stretched by 5 and 6 glass rods, respectively. In this way, about 7 cm^{-1} spectral resolution is achieved. The laser powers (the pump ~ 150 μW and the Stokes ~ 150 μW at the sample) are sufficiently low to ensure no damage of molecules or nanostructures during the experiments. A water immersion objective (Olympus, NA = 0.8, 40×) is used to focus the pump and the Stokes lasers on a sample. An oil condenser (Olympus, NA = 1.4) is used to collect the laser light in the forward direction. To obtain SRL signals, the Stokes beam is modulated at 2.2 MHz. Two 1000 nm short-pass filters block the Stokes laser before a photodiode with a lab-built resonant amplifier. To obtain SRG signals, the pump beam is modulated at 2.2 MHz. Two 1050/50 nm band-pass filters and two 1000 nm long-pass filters block the pump beam before the photodiode. A lock-in amplifier demodulates the SRS signals and the R channel is used to read out SRS signals. The hyperspectral PESRS datacube contains 200 × 200 pixels with 120 Raman channels. Each datacube took about 2 min with a 10 μs dwell time per pixel. The image area (30 μm × 30 μm) and pixel size (150 nm) are the same in all experiments. We note that Van Duyne's group used pump/Stokes and pump/anti-Stokes pulses to obtain SE-FSRG and SE-FSRL signals to sample different portions of LSPR of nanodumbbell colloids [12]. Here, we used the same pump and Stokes pulses and exchanged the modulated beam to obtain PESRL and PESRG to probe the same LSPR portions of the nanoparticle aggregation.

First, we compared the SRL and SRG responses of non-plasmonic enhanced SRS. Figure S3a shows SRL and SRG images of a solid adenine sample at the same location. The SRL and SRG spectra of adenine that are equal in the bandwidth and the Raman peak position are shown in Figure S3b. In principle, the SRL and the SRG signal are equal in magnitude. However, due to the wavelength-dependent quantum efficiency of the photodiode and different transmittances of filter sets, the SRL response in our microscope is about three times larger than the SRG response. The SRL and SRG response correction will be considered in the following results to ensure the PESRS spectra which could be compared accurately in magnitudes.

Next, we examined the PESRL and PESRG signals of the adenine adsorbed on Au NPs. 5 μL of a 1 mM aqueous adenine solution was added to 2–4 μL of concentrated 60 nm Au NPs colloid sol. Then, the Au NPs were dropped on a cover glass followed by vacuum drying. Crucially, the analytes induced the aggregation of Au NPs before drying, creating hot spots occupied by the analyte itself. We randomly measured three locations on the aggregated Au NPs substrate. Both PESRL and PESRG signals were collected in every location to avoid the interference of aggregation states. To decrease the intensity variation, the

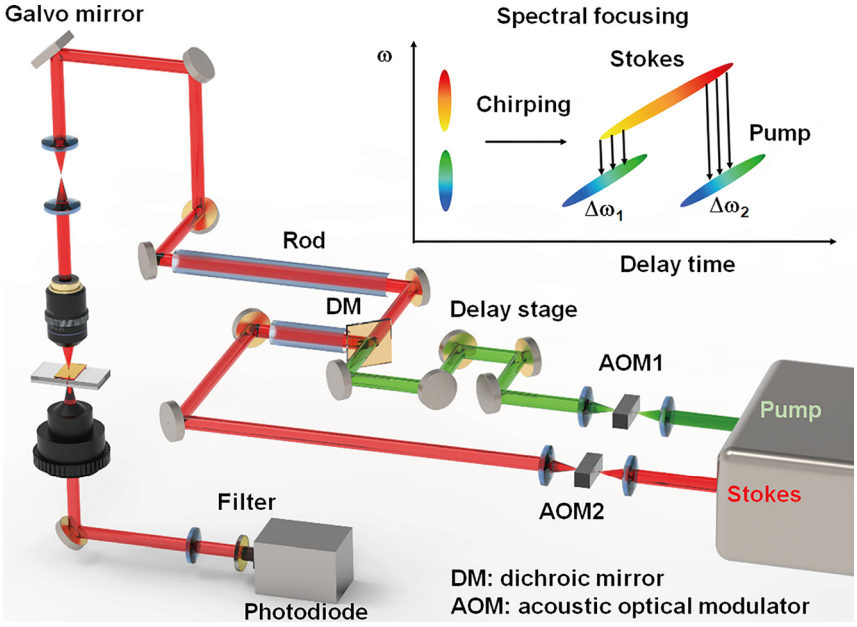

Figure 3: Schematic of spectral-focusing hyperspectral stimulated Raman scattering (SRS) microscope for stimulated Raman loss (SRL) and stimulated Raman gain (SRG) measurement.

PESRS spectra from all pixels in the whole image were averaged. The raw PESRL and PESRG spectra of adenine are displayed in Figure 4. The resulting PESRL spectra (Figure 4a) from the adenine-adsorbed Au NPs aggregates consists of a narrower feature at 727 cm^{-1} on the top of a strong and broad nonresonant background with a high end on the left. A penalized least squares fitting was used to subtract the broad spectral background [27]. The fitted backgrounds of PESRS are shown in Figure 4 as the same color dash lines. All PESRG spectra (Figure 4b) showed a broad background with a high end on the right and a sharp negative peak at 735 cm^{-1}. The end-for-end reversed backgrounds in PESRL and PESRG can be explained as following. For the PESRL measurement, the 969 nm laser is the "probe" beam and the modulated 1040 nm laser is the "heat" beam for the PT process. The "heat" and "probe" beam are exchanged with each other for the PESRG measurement, and relative delay time turns end for end. In this way, the PT decay profiles under two different conditions are just reversed. Additionally, the SRL and the PT effect both produce an intensity loss in the "probe" beam. Thus, the raw data of PESRL are the sum of the PT signal and the SRL signal. While the SRG is a "probe" beam gain process, the total signal is the subtraction of the SRG signal from the PT signal. Consequently, the PESRG appears as a negative peak on a broad PT background.

Figure 5 shows the vibrational resonant components of the PESRL and PESRG spectra obtained from the subtraction of the fitted backgrounds from the observed PESRS signals. For a better comparison, we set the strong peak of PESRG data as a positive peak. Due to our experimental conditions, the intensity of PESRL is about three times larger than that of PESRG. After the correction of the system response, the signal intensities are nearly identical between PESRL and PESRG. Remarkably, the PESRG result shows a blue shift in peak positions from the PESRL result and with an oppositely phased dispersion. In the PESRL result, the vibrational feature is characterized by a dip on the high wavenumber side and a peak on the low wavenumber side. While, in the PESRG result, the dip is on the low wavenumber side and the peak is on the high wavenumber side. This is an excellent agreement with our theoretical prediction of opposite dispersive line shapes between PESRL and PESRG.

Then, we simulated the spectra of adsorbed adenine on Au NPs based on eq. (8). The vibrational peak of adenine is at 731 cm^{-1} with a HWHM of 7 cm^{-1}. The PESRS spectra were simulated by using a plasmon response with $\Delta = 5000\ cm^{-1}$, $A = 100$, and $\Omega_R = 800$ nm. Experimentally, the enhancement factor of PESRS signal is about 10^6–10^7 in previous results [9, 13]. The PESRS signal is proportional to the cubic of the plasmonic field, as shown in our theory. Thus, here the value of A is selected as 100 for the simulation. The normalized simulated PESRL and PESRG are shown as green dot lines in Figure 5. For a better comparison, we set stimulated PESRL profile as a positive peak and show normalized PESRL and PESRG spectra. We find a good agreement in peak/dip positions and dispersive profiles between the experimental and simulated results. Simulated results also show a reversal in the sign of the dispersive PESRL and PESRG line shape. The excellent agreement between the experimental and simulated

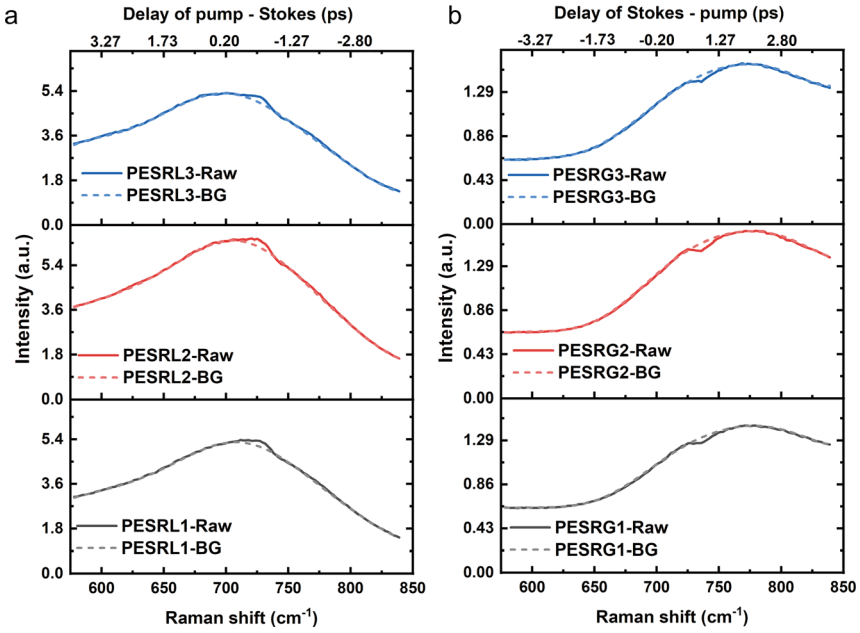

Figure 4: Three raw plasmon-enhanced stimulated Raman loss (PESRL) (a) and plasmon-enhanced stimulated Raman gain (PESRG) (b) spectra of adenine adsorbed on aggregated Au NPs which are obtained from different locations. Fitting backgrounds are displayed as dash lines.

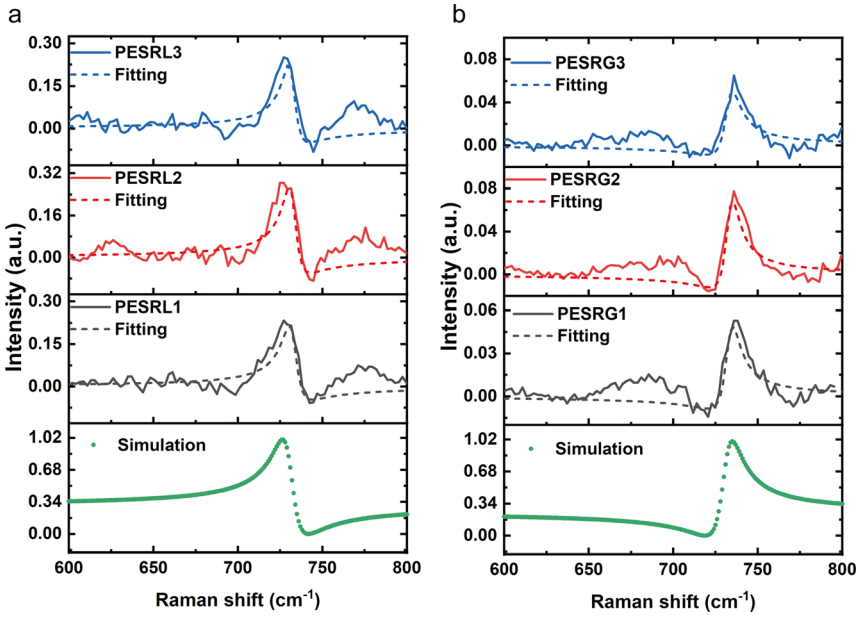

Figure 5: The experimental and simulated plasmon-enhanced stimulated Raman loss (PESRL) (a) and plasmon-enhanced stimulated Raman gain (PESRG) (b) spectra of adenine. The background-corrected PESRL and PESRG spectra are presented as solid lines (black, red, and blue). The Fano-like fitting spectral profiles based on eq. (9) are presented as the same color dash lines. Simulated PESRL and PESRG spectra based on eq. (8) are presented as green dot lines.

results collectedly confirms the reliability of our theoretical model.

In the literature, the Fano function has been used to describe a dispersive line shape of SE-FSRS [11]. As shown in eq. (8), the PESRS can be viewed as a linear combination of a Fano-line shape (the real part of the molecular susceptibility in which Fano parameter value is one as shown in eq. S1) and a Lorentzian line shape (the imaginary of the molecular susceptibility). For a better comparison with the Fano line shape, we insert eq. (3) into eq. (8) and the eq. (8) are reformatted into a Fano-like line shape as following:

$$I_{\mathrm{SRL}}^{\mathrm{PE}} = I_{\mathrm{PT}} - A_{\mathrm{SRL}}\left[\frac{\left(q_{\mathrm{SRL}} + \frac{\delta}{\Gamma}\right)^2}{1+\left(\frac{\delta}{\Gamma}\right)^2} - \frac{\left(\frac{\delta}{\Gamma}\right)^2}{1+\left(\frac{\delta}{\Gamma}\right)^2}\right] \tag{9a}$$

$$I_{\mathrm{SRG}}^{\mathrm{PE}} = I_{\mathrm{PT}} + A_{\mathrm{SRG}}\left[\frac{\left(q_{\mathrm{SRG}} + \frac{\delta}{\Gamma}\right)^2}{1+\left(\frac{\delta}{\Gamma}\right)^2} - \frac{\left(\frac{\delta}{\Gamma}\right)^2}{1+\left(\frac{\delta}{\Gamma}\right)^2}\right] \tag{9b}$$

where

$$q_{\mathrm{SRL}} = \frac{2\mathrm{Re}\,(F_P)}{\mathrm{Im}\,(F_P)} \tag{9c}$$

$$q_{\mathrm{SRG}} = -\frac{2\mathrm{Re}\,(F_S)}{\mathrm{Im}\,(F_S)} \tag{9d}$$

$$A_{\mathrm{SRL}} = |E_S F_S|^2 |E_P|^2 \frac{\mathrm{Im}\,(F_P)^2}{2\mathrm{Re}\,(F_P)\Gamma} \tag{9e}$$

$$A_{\mathrm{SRG}} = |E_P F_P|^2 |E_S|^2 \frac{\mathrm{Im}\,(F_S)^2}{2\mathrm{Re}\,(F_S)\Gamma} \tag{9f}$$

As shown in eq. (9), the PESRS profiles are the subtraction of two Fano profiles where the Fano parameter (q) of the first Fano function term depends on the real part and the imaginary part of plasmon enhancement coefficient and the Fano parameter of the second term is zero. The signs of the Fano parameters of PESRL and PESRG are opposite.

To valid this relation, we used the eq. (9) to fit the experimental spectra. We can obtain excellent agreements using $q = -1.7$ and $q = 2$ for all of the vibrational features in PESRL and PESRG, respectively. The fitting results are displayed in Figure 5 as the same color dash lines. The fitting results of the peak frequency, the bandwidth, and the amplitude are reported in Table S1. The reversal of the sign of q indicates an opposite change in the phase of dispersion between the PESRL and the PESRG process. Similar absolute values of q for PESRL and PESRG indicate approximate plasmonic responses due to the close wavelength of the pump and the Stokes beams in our experiments.

It is interesting to compare our phasor diagram and theoretical model to the SE-FSRS theories published by Ziegler and Schatz who only discussed the SRG process. In Ziegler's theory, the interference between Raman susceptibility and a stimulated surface plasmon emission results in asymmetric line shapes, and the increasing enhancement factors result in increasing dispersive line shapes [16]. In Schatz's theory, the Fano parameter depends on the ratio between the real part and the imaginary part of the square of the plasmonic field enhancement factor [17]. Different from Schatz's and Ziegler's work, our model makes an important prediction about the plasmonic enhancement factor which is given by $|F_S|^2 F_P$ and $|F_P|^2 F_S$ for PESRL and PESRG, respectively. The PESRS can be viewed as the result of the incoming propagating field interferences with the local plasmon-induced molecular dipole field having the same frequency as the incoming field. The incoming light plays the leading role in the far-field detection. This heterodyne detection is significantly different from surface-enhanced Raman scattering and surface-enhanced coherent anti-Stokes scattering, where the dipole re-radiation effect dominates the far-field contribution of the generated new frequency fields [28–30]. Different from Ziegler's work, we predict that PESRL and PESRG acquire the increasing dispersive character as the enhancement factor (A) increases and the dispersive character does not increase when the enhancement factor (A) reaches a certain level as shown in Figure 2a and b. As shown in Figures 1c and d and 2c and d, we predict more dispersive line shapes when the excitation laser wavelength is closer to the plasmon resonance peak. This prediction is qualitatively the same as the deduction from Schatz's work, not matching the previous frequency-dependent SE-FSRS results [12]. Up to now, all PESRS and SE-FSRS experiments were achieved on the ensemble measurements on aggregated NPs clusters. To better study the interaction between plasmon resonance and SRS process, the LSPR-depended experiment of a single particle or an individual hot spot is necessary to rule out the artifact of the ensemble measurements. The single nanorod or nanoshell with a tunable plasmonic peak can be potentially used. We also predict that abnormal pump beam intensity gain or Stokes beam intensity loss could happen in the plasmon post-resonance conditions. More importantly, a random substrate with various local LSPR responses leads to various local phases. This result implies that PESRS signals with different phases may cancel with each other, resulting in a decrease of the average intensity in the ensemble measurement of PESRS. A high-quality periodic substrate with a narrow distribution of LSPR could help improve the sensitivity of PESRS spectroscopy.

4 Conclusions

A theoretical model is developed to describe dispersive-like vibrational line shapes in PESRS microscopy. The plasmon-induced local electromagnetic field interacts with the molecular dipole, resulting in the dispersive line shapes of PESRS. The spectral feature further depends on the phase in the plasmonic field. Under the same laser and molecular conditions, an intensity loss in pre-plasmon resonance could become an intensity gain in post-plasmon resonance. At the same pump and Stokes wavelength setting, we experimentally observed PESRL and PESRG signals with reversed dispersive profiles, which fall into line with our theoretical prediction. We also verified that the nonresonant background in PESRS mainly originated from the photothermal effect. Together, we provided new insight into the nature of PESRS profiles and the mechanism of plasmonic enhancement of coherent Raman scattering. Results reported here can be used to improve signal enhancement in nanoscale coherent Raman imaging towards ultrasensitive detection of molecules.

Acknowledgments: We thank Lawrence D. Ziegler for his valuable suggestions in theory. We also thank Yurun Xie for his assistance with PESRS measurement.

Author contribution: All the authors have accepted responsibility for the entire content of this submitted manuscript and approved submission.

Research funding: This work was supported by NIH R01 grants GM118471, AI141439, and a Keck Foundation grant to J.X.C.

Conflict of interest statement: The authors declare no conflicts of interest regarding this article.

References

[1] Y. Shen, F. Hu, and W. Min, "Raman imaging of small biomolecules," *Annu. Rev. Biophys.*, vol. 48, pp. 347–369, 2019.

[2] R. C. Prince, R. R. Frontiera, and E. O. Potma, "Stimulated Raman scattering: from bulk to nano," *Chem. Rev.*, vol. 117, pp. 5070–5094, 2017.

[3] J.-X. Cheng and X. S. Xie, "Vibrational spectroscopic imaging of living systems: an emerging platform for biology and medicine," *Science*, vol. 350, p. aaa8870, 2015.

[4] L. Wei and W. Min, "Electronic preresonance stimulated Raman scattering microscopy," *J. Phys. Chem. Lett.*, vol. 9, pp. 4294–4301, 2018.

[5] L. Wei, Z. Chen, L. Shi, et al., "Super-multiplex vibrational imaging," *Nature*, vol. 544, p. 465, 2017.

[6] H. Xiong, L. Shi, L. Wei, et al., "Stimulated Raman excited fluorescence spectroscopy and imaging," *Nat. Photonics*, vol. 13, pp. 412–417, 2019.

[7] K. A. Willets and R. P. Van Duyne, "Localized surface plasmon resonance spectroscopy and sensing," *Annu. Rev. Phys. Chem.*, vol. 58, pp. 267–297, 2007.

[8] C. Zong, M. Xu, L.-J. Xu, et al., "Surface-enhanced Raman spectroscopy for bioanalysis: reliability and challenges," *Chem. Rev.*, vol. 118, pp. 4946–4980, 2018.

[9] R. R. Frontiera, A.-I. Henry, N. L. Gruenke, and R. P. Van Duyne, "Surface-enhanced femtosecond stimulated Raman spectroscopy," *J. Phys. Chem. Lett.*, vol. 2, pp. 1199–1203, 2011.

[10] L. E. Buchanan, N. L. Gruenke, M. O. McAnally, et al., "Surface-enhanced femtosecond stimulated Raman spectroscopy at 1 MHz repetition rates," *J. Phys. Chem. Lett.*, vol. 7, pp. 4629–4634, 2016.

[11] R. R. Frontiera, N. L. Gruenke, and R. P. Van Duyne, "Fano-like resonances arising from long-lived molecule-plasmon interactions in colloidal nanoantennas," *Nano Lett.*, vol. 12, pp. 5989–5994, 2012.

[12] L. E. Buchanan, M. O. McAnally, N. L. Gruenke, G. C. Schatz, and R. P. Van Duyne, "Studying stimulated Raman activity in surface-enhanced femtosecond stimulated Raman spectroscopy by varying the excitation wavelength," *J. Phys. Chem. Lett.*, vol. 8, pp. 3328–3333, 2017.

[13] C. Zong, R. Premasiri, H. Lin, et al., "Plasmon-enhanced stimulated Raman scattering microscopy with single-molecule detection sensitivity," *Nat. Commun.*, vol. 10, p. 5318, 2019.

[14] N. L. Gruenke, M. O. McAnally, G. C. Schatz, and R. P. Van Duyne, Balancing the effects of extinction and enhancement for optimal signal in surface-enhanced femtosecond stimulated Raman spectroscopy," *J. Phys. Chem. C*, vol. 120, pp. 29449–29454, 2016.

[15] B. Negru, M. O. McAnally, H. E. Mayhew, et al., "Fabrication of gold nanosphere oligomers for surface-enhanced femtosecond stimulated Raman spectroscopy," *J. Phys. Chem. C*, vol. 121, pp. 27004–27008, 2017.

[16] A. Mandal, S. Erramilli, and L. Ziegler, "Origin of dispersive line shapes in plasmonically enhanced femtosecond stimulated Raman spectra," *J. Phys. Chem. C*, vol. 120, pp. 20998–21006, 2016.

[17] M. O. McAnally, J. M. McMahon, R. P. Van Duyne, and G. C. Schatz, "Coupled wave equations theory of surface-enhanced femtosecond stimulated Raman scattering," *J. Chem. Phys.*, vol. 145, 2016, Art no. 094106.

[18] A. Fast and E. O. Potma, "Coherent Raman scattering with plasmonic antennas," *Nanophotonics*, vol. 8, pp. 991–1021, 2019.

[19] H. Rigneault and P. Berto, "Tutorial: Coherent Raman light matter interaction processes," *APL Photonics*, vol. 3, 2018, Art no. 091101.

[20] J.-X. Cheng and X. S. Xie, *Coherent Raman Scattering Microscopy*, Boca Raton, CRC Press, 2012.

[21] D. Zhang, M. N. Slipchenko, D. E. Leaird, A. M. Weiner, and J.-X. Cheng, "Spectrally modulated stimulated Raman scattering imaging with an angle-to-wavelength pulse shaper," *Opt. Express*, vol. 21, pp. 13864–13874, 2013.

[22] X. Hua, D. V. Voronine, C. W. Ballmann, A. M. Sinyukov, A. V. Sokolov, and M. O. Scully, "Nature of surface-enhanced coherent Raman scattering," *Phys. Rev. A*, vol. 89, 2014, Art no. 043841.

[23] A. Gaiduk, P. V. Ruijgrok, M. Yorulmaz, and M. Orrit, "Detection limits in photothermal microscopy," *Chem. Sci.*, vol. 1, pp. 343–350, 2010.

[24] M. Selmke, M. Braun, and F. Cichos, "Photothermal single-particle microscopy: detection of a nanolens," *ACS Nano*, vol. 6, pp. 2741–2749, 2012.

[25] S. Berciaud, D. Lasne, G. A. Blab, L. Cognet, and B. Lounis, "Photothermal heterodyne imaging of individual metallic nanoparticles: theory versus experiment," *Phys. Rev. B*, vol. 73, 2006, Art no. 045424.

[26] J. Olson, S. Dominguez-Medina, A. Hoggard, L.-Y. Wang, W.-S. Chang, and S. Link, "Optical characterization of single plasmonic nanoparticles," *Chem. Soc. Rev.*, vol. 44, pp. 40–57, 2015.

[27] Z.-M. Zhang, S. Chen, and Y.-Z. Liang, "Baseline correction using adaptive iteratively reweighted penalized least squares," *Analyst*, vol. 135, pp. 1138–1146, 2010.

[28] S.-Y. Ding, E.-M. You, Z.-Q. Tian, and M. Moskovits, "Electromagnetic theories of surface-enhanced Raman spectroscopy," *Chem. Soc. Rev.*, vol. 46, pp. 4042–4076, 2017.

[29] M. Kerker, D.-S. Wang, and H. Chew, "Surface enhanced Raman scattering (SERS) by molecules adsorbed at spherical particles: errata," *Appl. Opt.*, vol. 19, pp. 4159–4174, 1980.

[30] C. Steuwe, C. F. Kaminski, J. J. Baumberg, and S. Mahajan, "Surface enhanced coherent anti-stokes Raman scattering on nanostructured gold surfaces," *Nano Lett.*, vol. 11, pp. 5339–5343, 2011.

Supplementary Material: The online version of this article offers supplementary material (https://doi.org/10.1515/nanoph-2020-0313).